

Core/shell FeVO₄@BiOCl heterojunction as a durable heterogeneous Fenton catalyst for the efficient sonophotocatalytic degradation of p-nitrophenol

Eshaq Gh., Wang Shaobin, Sun Hongqi, Sillanpää Mika

This is a Final draft version of a publication
published by Elsevier
in Separation and Purification Technology

DOI: 10.1016/j.seppur.2019.115915

Copyright of the original publication: © 2019 Elsevier B.V.

Please cite the publication as follows:

Eshaq, Gh., Wang, S., Sun, H., Sillanpää, M. (2020). Core/shell FeVO₄@BiOCl heterojunction as a durable heterogeneous Fenton catalyst for the efficient sonophotocatalytic degradation of p-nitrophenol. Separation and Purification Technology, vol. 231. DOI: 10.1016/j.seppur.2019.115915

**This is a parallel published version of an original publication.
This version can differ from the original published article.**

Core/shell FeVO₄@BiOCl heterojunction as a durable heterogeneous Fenton catalyst for the efficient sonophotocatalytic degradation of p-nitrophenol

Gh. Eshaq^{a,b*}, Shaobin Wang^c, Hongqi Sun^d, Mika Sillanpää^a

a Department of Green Chemistry, School of Engineering Science, LUT University, Sammonkatu 12, FI-50130, Mikkeli, Finland

b Petrochemicals department, Egyptian Petroleum Research Institute (EPRI), Nasr City, Cairo 11727, Egypt

c School of Chemical Engineering, The University of Adelaide, SA 5005, Australia

d School of Engineering, Edith Cowan University, 270 Joondalup Drive, Joondalup, WA 6027, Australia

Abstract

In this study, a FeVO₄@BiOCl p–n heterojunction with n-type porous FeVO₄ nanorods as the core and p-type flower-like BiOCl nanostructures as the shell was successfully prepared by a facile hydrothermal method. The novel heterostructure was investigated as a durable heterogeneous Fenton catalyst for ultrasonic irradiation (US), ultraviolet irradiation (UV) and coupling irradiation systems (US/UV). Characterization of FeVO₄@BiOCl core shell heterojunction was conducted by XRD, SEM, EDS elemental mapping, TEM, HRTEM, SAED, FTIR, Raman, BET, PZC, XPS and DRS. Several different experimental parameters, including irradiation time, H₂O₂ concentration, catalyst amount, initial concentration, and pH value, were optimized. The stability and reusability of the prepared FeVO₄@BiOCl core shell heterojunction were evaluated as well. Mineralization experiments were carried out using the optimized parameters. The results showed that FeVO₄@BiOCl core shell heterojunction exhibits a superior sonophotocatalytic performance compared to either sonocatalysis or photocatalysis. Moreover, the formation of p-n core@shell nanostructures could significantly increase the pH_{pzc}, and to an excellent stability for the degradation of PNP after six cycles. The remarkable enhancement of

the degradation performance of FeVO₄@BiOCl core shell heterojunction can be attributed to the unique structure and morphology with a matched energy band structure owing to the internal electric field induced by the p–n junction, a high transfer efficiency and the efficient separation of e⁻/h⁺ pairs, resulting in a huge number of reactive species for the degradation of PNP. A plausible mechanism over FeVO₄@BiOCl core shell heterojunction for the sonophotocatalytic degradation of PNP is proposed based on a special three-way, i.e. one as a photocatalyst and a two-way Fenton-like mechanism with the dissociation of H₂O₂. Active species trapping and calculated band gap energy were also discussed.

Keywords: p-n heterojunction, sonophotocatalysis, synergistic effect, core shell, p-nitrophenol

1. Introduction

The wide use of nitro aromatic compounds as a synthetic intermediate in the manufacture of petrochemicals, pharmaceuticals, agrochemicals, fungicidal agents, plastics and preservatives [1], leads to an increased accumulation of phenolic compounds. Among the nitroaromatic compounds, p-nitrophenol (PNP) is an important intermediate in many industries such as the manufacturing of fine chemicals, dyes, explosives, industrial solvents and pesticides like bifenox, parathion, p-acetaminophenol and others [2, 3]. PNP was therefore found frequently in the wastewater effluents of these industries [4]. PNP has been classified as a priority pollutant by the United States Environmental Protection Agency (EPA), with a range of 1-20 ppb as a maximum allowed concentration in drinking water [5]. It is highly toxic to many living organisms, poses significant health and environmental risks and causes lung edema, central nervous system disorders, renal failure, skin, respiratory tract, myocardial depression and eye irritation [6]. PNP decays in surface water but, takes a long time in deep soil and in groundwater. PNP may also

accumulate in the food chain and in the surrounding environment [7, 8], so rapid degradation of PNP is indispensable. Many different methods including physical, chemical or biological treatment processes are carried out to remove PNP from wastewater. However these methods have their own limitations due to the high stability and refractory to conventional biological treatments of nitrophenol [9], and the accumulation of concentrated sludge creates a disposal problem even after phenols are removed [10].

Advanced Oxidation Processes (AOPs) have high degradation and mineralization efficiency for recalcitrant organic pollutants using highly reactive hydroxyl radicals. AOP techniques have facilitated different processes for oxidation reactions under benign conditions [11,12] such as classic Fenton, photocatalysis, photo-Fenton, ozonation and sonolysis, which are widely utilized in the oxidation of many organic pollutants [13]. Recently, a sonophotocatalytic system, combining US/UV of ultrasonic (US) and ultraviolet (UV) irradiation with a heterogeneous photocatalyst, can produce a huge number of hydroxyl radicals ($\cdot\text{OH}$), leading to the improved overall oxidation process [14]. Instead of using (US) or (UV) alone, sonophotocatalysis (US/UV) can significantly improve the degradation performance of recalcitrant organic pollutants synergistically and eliminate the disadvantages associated with each individual process [15]. For instance, the use of ultrasound in heterogeneous catalytic systems increases the turbulence in the liquid produced by acoustic cavitation, and can remove the disadvantages of the photocatalytic system such as a decrease in UV available sites, a decreased catalyst surface due to the blocking of the active sites by contaminants and mass transfer limitations [16]. De-aggregation and mass transfer, generation of hydroxyl radicals and catalyst particles as nuclei are the factors describing the performance of combined ultrasound and photocatalytic system that have been explained by Manickam et al. [17].

To date, semiconductor photocatalysts have attracted great attention because of their superior potential in water purification, environmental remediation and energy crisis [18, 19]. Recently, special attention has been paid to the design of rational semiconductor core shell nanoparticles, because of their unique structure and interesting properties by varying either the core constituent materials or the shell thickness [20, 21]. They are being widely utilized in catalytic, optical, electronic, magnetic, biotechnological, and sensing devices [22, 23].

More recently, semiconductor/semiconductor core shell nanostructures have received considerable research attention due to their high efficiency and superior stability. It is worth mentioning that this research has attracted great attention in the field of photocatalysis with a semiconductor heterojunction or core shell heterojunction, where both the core and shell are prepared from a semiconductor material or semiconductor alloy [24-27]. The main advantage of semiconductor/semiconductor core/shell nanostructures is an increase in photocatalytic activity and photooxidation stability, because they have an external coating of another semiconductor material [27]. The semiconductor hybrid combined between a narrow band gap and wide band gap can extend the range of light response and suppress the recombination rates of photoinduced electron-hole (e^-/h^+) pairs, resulting in enhanced photocatalytic activity [28]. Moreover, the good matching of crystal lattice and band gap between the two components, with the morphology into the heterojunction structure can greatly improve photocatalytic efficiency [29]. Among the most widely used semiconductors, iron vanadate ($FeVO_4$) is highly stable and has high photocatalytic degradation efficiency towards many organic pollutants [30]. $FeVO_4$ comprises earth-abundant elements and is considered as an n-type semiconductor, with low band gap energy at around 2.05 eV and visible light absorption in the range of up to 600 nm [31, 32]. As a result of the high recombination rate of the e^-/h^+ pairs and the narrow band gap, the

photocatalytic activity of FeVO₄ is not high enough, so the coupling of the n-type FeVO₄ narrow band gap with a p-type wide band gap semiconductor is an effective way to solve this problem. In addition, a wide band gap shell is able to protect the narrow band gap core from photocorrosion [33]. As one of the most important bismuth oxyhalides, bismuth oxychloride (BiOCl) is considered as a p-type wide band gap semiconductor ($E_g = 3.5$ eV) owing to its unique structure. BiOCl compound tends to crystallize in the tetragonal matlockite with a layer structure characterized by [Bi₂O₂]²⁺ slabs sandwiched between two slabs of Cl⁻ [34] with plate morphology and an ideal shell material [35]. BiOCl has more potential applications in UV photocatalysis for water splitting and organic compound decomposition [36, 37]. Furthermore, the coupling of the p-type, wide band gap of BiOCl and n-type, narrow band gap of FeVO₄ is a promising design to suppress the recombination of photo-induced e⁻/h⁺ pairs and to enhance the photocatalytic performance by a heterojunction structure [38, 39].

To the best of our knowledge, successful synthesis of a FeVO₄@BiOCl p-n heterojunction with a core shell nanostructure in which FeVO₄ as the core and BiOCl as the shell and its use as a Fenton-like catalyst for efficient sonophotocatalytic degradation of PNP in the presence of H₂O₂ have not been reported. In this work, a FeVO₄@BiOCl p-n heterojunction was synthesized and investigated with XRD, SEM, EDS, TEM, HRTEM, SAED, FTIR, Raman, N₂-adsorption-desorption, DRS and XPS. The different degradation parameters, for instance, irradiation time, catalyst loading, pH and H₂O₂ initial concentration were optimized, and the mineralization and recyclability were examined. Moreover, the synergistic effect with reaction kinetics was investigated in detail and the possible mechanism was discussed.

2. Experimental

2.1. Materials

Iron (III) chloride hexahydrate ($\text{FeCl}_3 \cdot 6\text{H}_2\text{O}$, 97 %), ammonium metavanadate (NH_4VO_3 , 99%), ethanol ($\text{C}_2\text{H}_5\text{OH}$, 99%), bismuth (III) nitrate pentahydrate ($\text{Bi}(\text{NO}_3)_3 \cdot 5\text{H}_2\text{O}$), potassium chloride (KCl) were purchased from Sigma Aldrich and used as received without purification. Milli-Q-purified water prepared in the laboratory was used for preparing all the solutions.

2.2. Catalysts preparation

2.2. Preparation of porous FeVO_4 nanorods

$\text{FeCl}_3 \cdot 6\text{H}_2\text{O}$ (2 mmol) was dissolved in 10 mL of deionized water and NH_4VO_3 (2 mmol) was dissolved in another 10 mL of deionized water at 90 °C. Next, the ammonium vanadate solution was added drop-wise to the ferric chloride solution under vigorous stirring. After 20 min of stirring, the obtained slurry was placed in a 50 mL Teflon-lined stainless-steel autoclave, which was sealed and heated at 180 °C for 3 h and then left to cool down naturally to the ambient temperature. The obtained precipitate was separated by centrifugation, washed with deionized water and absolute ethanol several times. After drying in an oven at 60 °C for 6 h, the obtained powder was calcined at 500 °C for 2 h at a heating rate of 5 °C/min [40].

2.3. Preparation of $\text{FeVO}_4 @ \text{BiOCl}$ p-n heterojunction with core shell nanostructures

$\text{FeVO}_4 @ \text{BiOCl}$ p-n heterojunction materials were prepared using a facile hydrothermal route, where 1 mmol $\text{Bi}(\text{NO}_3)_3 \cdot 5\text{H}_2\text{O}$ and 1 mmol KCl were dissolved in 40 mL of deionized water. After that, 0.15 g of the as-prepared FeVO_4 was added to the solution under continuous stirring. The suspension was placed in a 50 mL Teflon-lined stainless-steel autoclave, heated at 160 °C for 18 h, and then left to cool down naturally to the ambient temperature. The precipitates were separated by centrifugation, washed three times with deionized water and absolute ethanol, and then dried at 60 °C in a vacuum for 8 h [41].

2.4. Preparation of BiOCl

The preparation of BiOCl was the same as the synthesis of the FeVO₄@BiOCl core shell heterojunction nanostructures without adding FeVO₄.

2.5. Characterizations

A PANalytical diffractometer with Cu K α radiation (wavelength = 1.54 Å) was used to obtain the X-ray diffraction (XRD) for the crystallinity, phase composition, and purity of the prepared samples, operated at 40 kV and 40 mA in the range of $2\theta = 10-80^\circ$ at a scanning speed of $2\theta/\text{min}$ and 0.02° step size. A HITACHI /EDS S-4800 was operated at an accelerating voltage of 5 kV to obtain SEM images, attached to an energy-dispersive X-ray spectroscopy (EDS) detector for elemental mapping of composition analysis. A TEM JEOL JEM-2010 (HT) operated at 200 kV was used for TEM images, (HRTEM) and (SAED). A Horiba Jobin Yvon, and Labram HR with a green laser at wavelength 514.5 nm was recorded at room temperature, and a Bruker Platinum ATR VERTEX 70 was used to determine Raman and FTIR spectra, respectively. A MicroActive-TriStar II Plus 2.03 analyzer was used to obtain the BET surface area. Point of zero charge (PZC) was determined using the mass titration method [42]. An ESCALAB 250Xi with Al-K (1486.6 eV) as the X-ray source was used to measure the XPS of the prepared catalysts. An Agilent UV-vis spectrophotometer (Cary 5000) with a DRA 2500 integrating sphere was used to measure the DRS and elucidate the absorption profiles of the prepared catalysts with BaSO₄ attached on a black carbon tape as the reference.

2.5. Sonophotocatalytic degradation

A Sonics & Materials, Inc. VCX 750 ultrasonic instrument was used to execute all ultrasonic operations, during which a constant frequency of 20 kHz attached to a titanium probe with a tip diameter of 13 mm and power output of 125 W was employed as a source of US

irradiation. During the entire sonocatalytic experiment, the tip of the probe was immersed below the PNP solution surface by about 2 cm. For the PNP photodegradation experiments, a UV lamp (shortwave, 254 nm, 8 watt, Analytik Jena, Germany) was adjusted parallel to the quartz double jacket reactor with a constant distance between them. When the photocatalysis experiments were carried out, a magnetic stirrer adjusted to 500 rpm was used and the sonicator was turned off. While the UV lamp was turned off, sonocatalytic experiments were carried out. In addition, the water circulation system was used to maintain the reaction temperature at 25 ± 2 °C. In each experiment, the PNP solution was 110 mL, followed by dispersion of a certain amount of catalyst into the solution. The reaction was started at once by adding the hydrogen peroxide to the PNP solution and turning on the US, UV lamp or combined US/UV. After the irradiation was completed, 1 mL of aliquots was withdrawn at intervals and the catalyst was immediately removed by filtration with a 0.45- μ m-pore-size membrane syringe filter. Samples were analyzed using an HPLC (SHIMADZU®) equipped with a Phenomenex® C18 column (5 μ m, 150 mm \times 4.6 mm) and a UV detector set at 285 nm. A mixture of acetonitrile and Milli-Q water with a volumetric ratio of 50:50 was degassed in an ultrasonic bath and passed through a Millipore filtration apparatus (0.2 μ m) before being used at a flow rate of 1 mL/min as the mobile phase throughout the analysis. The injection flow rate was kept at 1 mL/min. A Total Organic Carbon Analyzer (TOC-VCPH Shimadzu) equipped with an auto sampler (ASI-V Shimadzu) was used for the mineralization analysis. All experimental were performed with at least three replicates. Data were reported as average \pm standard deviations.

3. Results and discussion

3.1. Characteristics of the samples

3.1.1. XRD

The crystallographic and structure studies of the prepared samples of FeVO₄, BiOCl and FeVO₄@ BiOCl p-n heterojunction were detected by XRD. As shown in Fig. 1, the FeVO₄ corresponded to the standard triclinic FeVO₄ (JCPDS No. 71-1592) and no other diffraction peaks were detected. The XRD pattern of the BiOCl corresponded to the standard tetragonal BiOCl (JCPDS card No. 85-0861). The coexistence of all characteristic peaks of both FeVO₄ and BiOCl in Fig. 1 indicates that the FeVO₄@BiOCl p-n heterojunction is composed of triclinic FeVO₄ and tetragonal BiOCl. No additional impurity phases were found in the diffraction patterns of FeVO₄@BiOCl p-n heterojunction core shell nanostructures, suggesting that the FeVO₄@BiOCl core shell exhibit a coexistence of both FeVO₄ and BiOCl phases. According to the Scherrer equation, the calculated crystallite sizes of FeVO₄, BiOCl and FeVO₄@BiOCl p-n heterojunction were estimated to be 45, 25 and 73 nm, respectively. This indicates that the FeVO₄ inner core semiconductor, which was prepared at first, has a crystallite size much larger than that of the BiOCl semiconductor shell layer.

3.1.2. SEM - EDS with elemental mapping

The morphology of FeVO₄, BiOCl and FeVO₄@BiOCl p-n heterojunction were investigated by SEM (Fig. 2 (a-c)). The SEM image of FeVO₄ exhibits a uniform porous nanorod-type with smooth surfaces while BiOCl exhibits a flower-like structure with a lot of BiOCl petals inserted. The SEM image of Fig. 2 (c) clearly shows the core shell nanostructures, where the porous nanorod particles of FeVO₄ are surrounded by a thin layer of BiOCl nanoparticles. However, the FeVO₄@BiOCl p-n heterojunction core shell nanostructures become rough after the BiOCl shell growth, indicating the surface of the porous nanorod particles of FeVO₄ coated with BiOCl nanoparticles. The successful synthesis of the FeVO₄@BiOCl p-n

heterojunction core shell nanostructures was further confirmed by the chemical composition measured by EDS as displayed in Fig. 2 (d). The EDS spectrum indicates that the main peaks are Fe, V, O, Bi and Cl. A magnified SEM image shows the selected area of FeVO₄@BiOCl p-n heterojunction core shell nanostructures. This result confirmed that the final product was of a highly pure FeVO₄@BiOCl p-n heterojunction core shell nanostructure. Moreover, Fig. 2 (f-j) shows the elemental mappings of the FeVO₄@BiOCl p-n heterojunction core shell nanostructures. The results confirmed the homogenous distribution of Fe, V, O, Bi and Cl elements in the core shell heterojunction.

3.1.3. TEM, HRTEM and SAED

To obtain further convincing evidence about the composition of the core shell nanostructures, the catalysts were characterized by TEM, HRTEM and SAED analysis. Fig. 3 (a-c) shows the TEM images of FeVO₄, BiOCl and FeVO₄@BiOCl p-n heterojunction, respectively. As shown in Fig. 3 (a), FeVO₄ shows morphology of porous nanorods in an average diameter of 45-50 nm with smooth surfaces, while in Fig. 3 (b) BiOCl shows well-defined flower-like architectures with an average particle size of 20-30 nm. The particle size results agree well with the data calculated by the Scherrer equation. However, Fig.3 (c) shows a FeVO₄ core nanorod with a diameter of ~50 nm and the surrounding BiOCl shell with an average thickness of ~20 nm. The difference in brightness between the core and the shell in the magnified TEM image clearly endorses the formation of core shell nanostructures. The corresponding SAED pattern of FeVO₄, BiOCl and FeVO₄@BiOCl p-n heterojunction are displayed in Fig 3 (d-f). The rings observed in Fig.3 (d, e) suggest the presence of a single crystalline phase of the triclinic FeVO₄ and tetragonal crystal structure of BiOCl. The bright spots corresponding to BiOCl were observed with a high crystallinity (Fig.3(f)), corroborating evidence of the formation of core

shell geometry in FeVO₄@BiOCl nanostructures. The HRTEM image of FeVO₄@BiOCl core shell heterojunction is shown in Fig. 3 (g) and different lattice fringes can be observed. The lattice fringes of 0.624 nm correspond to the interplanar spacing of (111) plane of the triclinic FeVO₄ phase, while the lattice fringes of 0.275 nm belong to the (110) crystalline plane of tetragonal BiOCl.

3.1.4. FTIR

To identify the functional groups presented in the prepared catalysts, FTIR was performed (Fig 4.) In the FTIR spectra, the characteristic bands in the regions 1,650 and 3,400–3,700 cm⁻¹ are attributed to physically adsorbed water. The spectrum of FeVO₄ can be divided into four different groups: (1) Terminal V–O stretching in the range of 970–895 cm⁻¹, (2) bridging V–O–Fe stretching in the range of 890–736 cm⁻¹, (3) mixed bridging V–O–Fe and V–O–Fe stretching in the range of 730–633 cm⁻¹ and (4) V–O–V deformations and Fe–O stretching in the range of 502–317 cm⁻¹. Each band could be attributed to one of these groups by comparison with values reported in previous literature [43, 44]. The FTIR spectrum of BiOCl only shows a very strong band at 524.54 cm⁻¹ which is attributed to the Bi–O bond [45]. In the case of FeVO₄@BiOCl p-n heterojunction, the characteristic bands for both FeVO₄ and BiOCl were found. Interestingly, the FeVO₄@BiOCl spectrum clearly shows that the intensity of the BiOCl band is greatly enhanced and the peak is broadened due to the overlap of the IR band of FeVO₄ with BiOCl. Thus, the FTIR analysis shows the coexistence of FeVO₄ and BiOCl in the core shell nanostructures.

3.1.5. Raman

Further evidence of core shell heterojunction formation in FeVO₄@BiOCl nanostructures is revealed by Raman spectroscopy. The Raman spectra of FeVO₄, BiOCl and FeVO₄@BiOCl p-n heterojunction are shown in Fig. 5. The Raman spectrum of FeVO₄ shows the characteristic bands of pure FeVO₄, which concur with the data given with previous reports [46, 47]. The Raman spectrum of BiOCl exhibits bands at 61.5, 139.5 and 192.2 cm⁻¹, corresponding to Bi–Cl stretching modes, and the band at 390 cm⁻¹ is attributed to the Bi–O stretching mode [48]. In the case of FeVO₄@BiOCl p-n heterojunction, the characteristic peaks for both the FeVO₄ and BiOCl were found. Furthermore, the intensity of the bands is greatly enhanced and the peaks are broadened due to the overlap of FeVO₄ with the bands of BiOCl.

3.1.6. N₂ adsorption-desorption isotherm.

N₂ sorption isotherms of FeVO₄, BiOCl and FeVO₄@BiOCl p-n heterojunction and pore size distributions (BJH) are displayed in Fig. 6. The isotherms of all the catalysts are type-IV adsorption isotherms with an H3 hysteresis loop according to the IUPAC classification [49]. The BJH curves reveal the presence of the mesoporous region in the range of (10-50 nm) for all the catalysts Fig. 6, inset. The surface areas (S_{BET}) calculated using the BET equation [50], total pore volume, V_p taken at P/P₀ = 0.95, and average pore radius are listed in Table 1. The S_{BET} values of FeVO₄ and BiOCl are 24.2 m² g⁻¹ and 11.3 m² g⁻¹, respectively, while the surface area of FeVO₄@BiOCl p-n heterojunction is 71.6 m²/g, which is approximately 3 times greater than FeVO₄ and is much greater than BiOCl. The enhanced surface area stemming from the rough surface of core shell heterojunction could facilitate more surface active sites. These results revealed that the growth of BiOCl shell onto the porous nanorod particles of FeVO₄ greatly enhances the surface area of resulting FeVO₄@BiOCl core shell heterojunction. Moreover, the FeVO₄@BiOCl p-n heterojunction also shows approximately 3 times greater in total pore

volume of $0.11 \text{ cm}^3 \text{ g}^{-1}$ compared to that of FeVO_4 ($0.032 \text{ cm}^3 \text{ g}^{-1}$) and BiOCl ($0.028 \text{ cm}^3 \text{ g}^{-1}$). The results indicated that the formation of BiOCl shell onto the FeVO_4 nanorods significantly increases the surface area of single-component material. Such a large surface area and total pore volume could facilitate mass transfer of the reactants, enhance the incident light harvesting and increase surface active sites [18,51], leading to a higher catalytic activity.

3.1.7. Diffuse reflectance spectroscopy (DRS)

The UV–vis diffuse reflectance spectra and band gap of FeVO_4 , BiOCl , and $\text{FeVO}_4@ \text{BiOCl}$ p-n heterojunction in the range of 250-800 nm are shown in Fig. 7(a). BiOCl shows strong absorption of ultraviolet light with an absorbance edge of 360 nm, while FeVO_4 and $\text{FeVO}_4@ \text{BiOCl}$ p-n heterojunction show good absorption in the visible light range with an absorbance edge around 600 and 650 nm, respectively. The band gap energy of the crystalline semiconductors can be obtained from the intercept of the straight-line portion of the plot of the modified Kubelka–Munk function $[F(R_\infty)hv]^{1/2}$ versus the energy of the absorbed light (hv) [52]. Fig. 7(a) shows that the band gap energies of FeVO_4 and BiOCl were estimated to be 1.95, and 3.46 eV, respectively. However, $\text{FeVO}_4@ \text{BiOCl}$ p-n heterojunction exhibits an obvious shift of absorption edge toward the visible region at 1.90 eV. To estimate the transition character of the adsorption edge (direct or indirect), we measured the shape of the reflectance spectra. In semiconductors, the square of the absorption coefficient is linear with energy for direct optical transitions in the absorption edge region, whereas the square root of the absorption coefficient is linear with energy for indirect transitions. As shown in Fig. 7(b), the absorption^{1/2} versus energy plot is nearly linear, while absorption² versus energy deviates from the fitted straight line. This feature suggests that the absorption edges of the samples are caused by indirect transitions.

2.1.8. XPS

To obtain further convincing proof of the core shell heterojunction, XPS analysis was performed to investigate the oxidation state and surface composition of the samples Fig.8 (a),(b). The XPS patterns of FeVO₄@BiOCl before sonophotocatalytic treatment are shown in Fig. 8(a). The XPS survey spectrum of FeVO₄@BiOCl p-n heterojunction shows the presence of C, Fe, O, V, Bi and Cl. The C 1s peak located at 284.5 eV can be ascribed to the signal from carbon contained in the instrument and was used for calibration [53]. The peaks at 723.65 and 710.4 eV are assigned to the Fe 2p_{1/2} and Fe 2p_{3/2} signals of the Fe³⁺ species [54]. The characteristic spin-orbit splitting of V 2p_{1/2} and V 2p_{3/2} signals was observed at approximately 524.0 and 517.2 eV, respectively, attributed to V⁵⁺ in FeVO₄, and O 1s signals at a binding energy of 531.77 eV correspond to the O²⁻ [55, 56]. In addition, the two characteristic peaks for Bi 4f, located at 164.4 and 159.0 eV, are attributed to Bi 4f_{5/2} and Bi 4f_{7/2}, respectively, confirming that the bismuth species in the heterojunction is Bi³⁺ [57,58]. For the spectra of Cl 2p, the peaks with binding energies at 197.6 and 199.2 eV are ascribed to Cl 2p_{3/2} and Cl 2p_{1/2}, respectively, indicating the characteristic of Cl⁻ [59]. According to the XPS results, the coexistence of FeVO₄ and BiOCl in the core shell nanostructures can be further confirmed. XPS spectra of FeVO₄@BiOCl core shell nanoparticles after sonophotocatalytic treatment are shown in Fig. 8(b). The result demonstrate that there is no obvious change of XPS spectra of the FeVO₄@BiOCl before and after sonophotocatalytic treatment and the presence of Fe⁺³/Fe²⁺, V⁵⁺/V⁴⁺ cycles reveal that hydroxyl radicals generated under heterogeneous Fenton like mechanism.

3.2. Degradation of PNP using ultrasonic or ultraviolet in the presence of FeVO₄@BiOCl p-n heterojunction core shell nanostructures

3.2.1. Insight into sonolysis (US) and photolysis (UV) conditions

Initially, an investigation of the impact of either sonolysis (at an extremely high temperature and pressure produced by acoustic cavitation bubbles implosion, which produces $\cdot\text{OH}$ and $\cdot\text{H}$ as a result of the pyrolysis of water molecules) or photolysis alone (a considerable number of $\cdot\text{OH}$ are generated through the photolysis of water) [60, 61] on the degradation of PNP in the absence of any catalyst was performed to determine the degradation efficiency of the (US) and (UV) irradiation. The extents of degradation after 60 min of sonication or ultraviolet irradiation were only 19% and 28%, respectively, as shown in Fig. S1. The effect of H₂O₂ concentration on the (US) and (UV) of PNP was investigated in the range of 5 – 40 mM Fig.S2). The degradation efficiencies reached 35% and 54% at 20 mM H₂O₂ for US and UV, respectively, but the degradation efficiency decreased with a further increase in H₂O₂ beyond this concentration. The enhancement of the degradation efficiency upon the addition of hydrogen peroxide is attributed to enrichment in the generation of $\cdot\text{OH}$ [62]. Moreover, the cleavage of the bond energy O–O (139 kJ mol⁻¹) in H₂O₂ is much easier than that of the bond energy O–H (463 kJ mol⁻¹) of water [63]. However, the suppression of degradation efficiency upon the continuous addition of an excessive amount of H₂O₂ leads to more scavenging of hydroxyl radicals and the generated free radicals [17], which indeed retard the degradation of organic compounds by consuming more H₂O₂ and the radical species generated by the decomposition of H₂O₂ would be finally terminated to produce O₂ and H₂O which ascribed to the scavenging phenomenon of $\cdot\text{OH}$ [64].

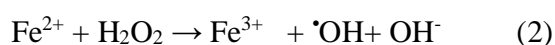
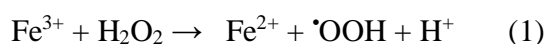
3.2.2. Influence of ultrasonic or photo-heterogeneous Fenton

In order to probe the capability of FeVO₄@BiOCl p-n heterojunction, some experiments were performed in the absence of (US) or (UV) irradiation. It can be seen that the degradation efficiency reached 11% using 0.1 g L⁻¹ of the catalyst, 40 mM of H₂O₂, PNP (20 ppm) at pH 7 and after 1 h stirring. The result indicates that the turbulence of the solution has little degradation efficiency.

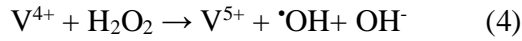
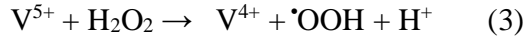
3.2.2.1. Influence of sonocatalytic or photocatalytic irradiation time

The prepared FeVO₄@BiOCl core shell heterojunction was introduced as heterogeneous Fenton catalysts to the sonolysis or photolysis systems in the presence of H₂O₂, and the effect of irradiation time was investigated (Fig. S3). Using 0.1 g L⁻¹ of FeVO₄@BiOCl heterojunction, 10 mM of H₂O₂, PNP (20 ppm), pH 7 and 1 h time for irradiation, degradation extents of 80% and 90% were achieved for US and UV, respectively.

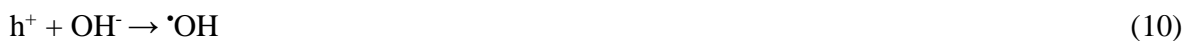
To gain a detailed understanding of the plausible sonocatalytic degradation mechanism of PNP over the FeVO₄@BiOCl p-n heterojunction, the mechanism of Fenton-like reaction was studied. The catalytic mechanism was possibly involved in a special two-way Fenton-like mechanism, which is the dissociation of H₂O₂ by both Fe³⁺ and V⁵⁺ in FeVO₄ to generate active hydroxyl radical [•]OH. The two-way Fenton-like mechanism can be described as follows in the equations [65]:



The activation of V^{5+} in $FeVO_4$ with H_2O_2 to generate hydroxyl radicals is described in the following equations. [66, 67]:



According to the above equations, the two-way catalytic mechanism involved in the Fe^{+3}/Fe^{+2} and V^{+5}/V^{+4} redox cycles takes place in the $FeVO_4-H_2O_2$ system as shown in eq. (1)–(2) and (3)–(4). We believed that these two redox cycles (Fe^{+3}/Fe^{+2} and V^{+5}/V^{+4}) were more able to consider $FeVO_4$ as a highly active Fenton-like catalyst than the conventional heterogeneous catalysts such as magnetite [65]. On the other hand, the radicals production in the sonocatalytic degradation of PNP using BiOCl in $FeVO_4@BiOCl$ p-n heterojunction occurs by a different mechanism, through a phenomenon called sonoluminescence [68]. The sonoluminescence occurring through ultrasonic irradiation could be emitting light within a wide wavelength range [69, 70]. The generation of the reactive oxygen species (ROS) via the sonoluminescence phenomenon over BiOCl in the presence of US is illustrated in the following equations [71]:



It can thus be concluded that the sonocatalytic degradation mechanism of PNP over $FeVO_4@BiOCl$ p-n heterojunction core shell nanostructures could be ascribed to a special two-

way Fenton-like mechanism and the dissociation of H₂O₂ by both Fe³⁺ and V⁵⁺ in FeVO₄ and the sonoluminescence phenomenon.

We believe that, when semiconductors are used as a catalyst, there is a similar plausible mechanism between sonocatalytic and photocatalytic degradation, so the recombination of electron-hole pairs should be suppressed to enhance the catalytic performance.

The band edge potential plays a crucial role in estimating the transfer of photoinduced charge carriers in a p-n heterojunction. To approach the photocatalytic mechanism of FeVO₄@BiOCl p-n heterojunction core shell nanostructures, the relative band positions of the FeVO₄ and BiOCl were investigated. The Mulliken electronegativity theory was used to determine the band edge positions of the conduction band (CB) and the valance band (VB) at the value of PZC as expressed in the following equation [72, 73]:

$$E_{CB} = \chi - E_e - 1/2E_g \quad (11)$$

$$E_{VB} = E_g + E_{CB} \quad (12)$$

where χ is absolute electronegativity of the semiconductor, E_e is the free electron energy on the hydrogen scale (ca. 4.5 eV), and E_g represents the band gap energy. The calculated values of both CB and VB of FeVO₄ are -0.44 and 1.56 eV, and those of BiOCl are 0.15 and 3.53 eV, respectively. Monoclinic FeVO₄ is a typical n-type semiconductor with a Fermi level lying close to CB, whereas BiOCl exhibits the characteristic properties of a p-type semiconductor where the Fermi level is located close to the VB. Before the formation of the FeVO₄@BiOCl p-n heterojunction, the CB edge of p-BiOCl is lower than that of n-FeVO₄, and the Fermi level of the BiOCl is also lower than that of the FeVO₄. When FeVO₄ nanorods are in contact with BiOCl, the electron will diffuse from n-FeVO₄ to p-BiOCl, causing the accumulation of negative charges

in the BiOCl region. At the same time, holes will diffuse from p-BiOCl to n-FeVO₄, resulting in a positive charged region near FeVO₄. The diffusion of electrons from n-FeVO₄ to p-BiOCl stops when the Fermi levels align and reach the thermal equilibrium state [74]. Meanwhile, the energy band positions of p-BiOCl are raised up along the Fermi level ($E_{f,p}$) and those of n-FeVO₄ are lowered along their Fermi level ($E_{f,n}$). As a result, the CB bottom of p-BiOCl became higher than that of n-FeVO₄ owing to the formation of the FeVO₄@BiOCl p-n junction. With FeVO₄ and BiOCl being closely joined together and after the FeVO₄@BiOCl p-n junction formed, an internal static electric field from n-FeVO₄ to p-BiOCl was established at the heterojunction interfaces [75]. Under UV-light irradiation, both FeVO₄ and BiOCl absorb photons of energy greater than the corresponding band gap energy, which helps excite the electrons in the VB to the CB and leave holes in the VB. According to the effect of the internal static electric field, the excited electrons are transferred from the CB of the p-BiOCl to the CB of the n-FeVO₄. And simultaneously the holes prefer to stay in the VB of p-BiOCl [76]. As a consequence, the photoelectrons in the CB of the n-FeVO₄ can be trapped by (O₂) molecules to produce reactive super oxide radicals (O₂^{•-}), and holes are remained in the VB of BiOCl reacting with H₂O to produce a large amount of •OH radicals [77] or directly react with the reactants adsorbed on the surface of the photocatalyst [74, 78]. In other words, the holes in the VB of BiOCl could initiate oxidation reactions, and the excited electrons in the CB of FeVO₄ could simultaneously create a reduction reaction. Therefore, the internal field created by the II-type p-n heterojunction with matched band edge potentials of FeVO₄ and BiOCl greatly promotes the separation of photogenerated electron-hole pairs between p-BiOCl and n-FeVO₄ and enhances the photocatalytic performance through spatially selective oxidation and reduction [79], the

formation of FeVO₄@BiOCl p-n heterojunction and the energy band structure are presented in Scheme 1.

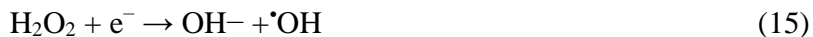
Scheme 1 (a) The band energy of n-FeVO₄ and p-BiOCl before contact and (b) formation of FeVO₄@BiOCl p-n junction and the proposed charge separation process and transfer mechanism under UV-light irradiation and plausible mechanism for the sonophotocatalytic degradation of PNP.

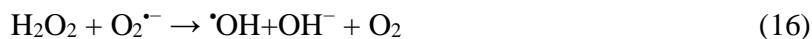
3.2.2.2. Influence of H₂O₂ concentration

The addition of hydrogen peroxide in the range of 5 – 40 mM promotes the degradation efficiency of PNP up to a certain amount of H₂O₂, for US 15 mM, and for UV 20 mM as shown in Fig.S4. A remarkable improvement in degradation efficiency was related to the decomposition of H₂O₂ to produce [•]OH under US or UV irradiation. Hydrogen peroxide is considered highly relevant in the catalytic degradation domain and plays a vital role in the enhancement of degradation efficiency. It is obvious that H₂O₂ dissociates to produce [•]OH under US or UV irradiation, but PNP degradation efficiency was slightly inhibited with excessive amounts of hydrogen peroxide. This can be attributed to the scavenger effects of [•]OH by H₂O₂, as described in the following Eq. (13) and (14).



On the other hand, hydrogen peroxide also acts as electron traps. H₂O₂ reacts with e⁻ in the (CB), thus suppressing the e⁻/h⁺ recombination [80], as can be described in Eq. (15), (16):





3.2.2.3. Influence of catalyst amount

To unfold the optimal amount of the catalyst for the degradation of PNP, different catalyst amounts in the range of 0.05–1 g L⁻¹ of FeVO₄@BiOCl p-n junction were tested, as shown in Fig.S5 for US and UV irradiation. The degradation efficiency is enhanced by increasing the amount of catalyst up to 0.3 g L⁻¹, and then any further increase in catalyst amount reduces the degradation capability of the system. As the catalyst amount increases, the number of the active sites increases, which enhances the rate of cavitation bubble generation and greater H₂O₂ decomposition to produce a huge number of $\cdot\text{OH}$ [81,82]. However, the degradation efficiency decreases upon increasing the catalyst amount, due to the scattering of ultrasound irradiation and the blocking of the transmission of ultrasound waves and energy near the catalyst surface, which in turn decreases degradation efficiency [83]. Moreover, the opacity and screening effect of the agglomerated catalyst prevents the penetration of UV light from illuminating the catalyst particles, which in turn decreases degradation efficiency [84].

3.3. Optimization of the sonophotocatalytic degradation of 4-NP using FeVO₄@BiOCl p-n core shell junction

To evaluate the effect of sonophotocatalytic degradation using a small amount of the catalyst and hydrogen peroxide in the shortest irradiation time with all the optimized parameters, sonocatalytic and photocatalytic reactions were carefully selected and applied in the sonophotocatalytic system and the results are shown in Fig.9. Complete degradation of 20 ppm of PNP using 0.1 g L⁻¹ of FeVO₄@BiOCl in the presence of 10 mM H₂O₂ and pH = 7 at room temperature will be achieved in 40 min. The degradation performance of the sonophotocatalytic

system was higher than that of the sonocatalytic or photocatalytic system by 26% and 20%, respectively and the performance ordered is sonophotocatalysis > photocatalysis > sonocatalysis. This remarkable performance can be ascribed to the ability of the combined irradiation system US/UV to overcome all the disadvantages observed in the individual systems, such as the blocking of the catalyst active sites and catalyst fouling [85]. It is worth mentioning that the accompanying irradiation system US/UV has many advantages such as increased production of hydroxyl radicals, enhanced mass transfer limitation [86,87,88], and enhanced catalytic activity due to catalyst dispersion and the prevention of the aggregation of the catalyst particles, as well as increasing surface area [89,90].

3.3.1. Synergistic effect and kinetic study

The synergistic effects of using sonocatalytic system, photocatalytic system and sonophotocatalytic system were studied and obtained by calculating the difference between the sonophotocatalytic degradation rate constant and the sum of rate constants of the use of sonocatalysis and photocatalysis individually Eq. (17) [91].

$$\text{synergy (S\%)} = \frac{(\mathbf{k_{sonophotocatalysis}} - (\mathbf{k_{sonocatalysis}} + \mathbf{k_{photocatalysis}}))}{\mathbf{k_{sonophotocatalysis}}} \times 100 \quad (17)$$

The sonophotocatalytic degradation of PNP follows the pseudo first order and the degradation rate constant for the combined irradiation system US/UV is found to be higher than the sum of the degradation rate constant of each system under the same conditions as shown in Table 2 and Fig.S6. Furthermore, a synergetic effect value greater than 1 indicates a positive synergistic

effect in using the hybrid system US/UV on PNP degradation performance. It was seen that the mechanism of US and UV provides us with a full description of the sonophotocatalytic mechanism of PNP degradation using FeVO₄@BiOCl p-n heterojunction, so the results of this study suggest strongly that the superior performance of FeVO₄@BiOCl p-n junction can be attributed to the morphological design and appropriate band alignment that improves the transfer and separation of e⁻/h⁺ pairs within the p-n heterojunction (Scheme 1(b)).

3.3.2. Influence of initial pH

To evaluate the effect of initial pH on the sonophotocatalytic system, a wide pH range of 2.7 - 11 was screened as shown in Fig.S7. Complete degradation of PNP at the different pH values is achieved after only 40 min, showing that the working pH range of FeVO₄@BiOCl core shell heterojunction can be extended to alkaline pH range (pH = 9). The pK_a value of PNP is 7.15, so it is negatively charged at above this pH value and positively charged below the pH [92,93]. The FeVO₄@BiOCl core shell heterojunction successfully overcomes the narrow working pH range in the heterogeneous Fenton process. This is due to the presence of V⁵⁺ in FeVO₄ as a Lewis acid that adsorbs OH⁻ in solution and decreases solution pH values in the system [94]. This increases the affinity to protons, leading to an increase in the pH_{PZC} of FeVO₄@BiOCl p-n junction relative to either FeVO₄ or BiOCl. The zeta potentials of FeVO₄, BiOCl and FeVO₄@BiOCl p-n junction were estimated using the mass titration method (Fig.S8). The PZC of FeVO₄@BiOCl p-n junction is higher than that of FeVO₄ and BiOCl with values of 9.8, 8.1 and 8, respectively. The enhanced PZC reveals that FeVO₄@BiOCl core shell heterojunction could invert the surface negative charge to positive, eliminating the electrostatic repulsion of PNP at higher pH values [95]. It can thus be concluded that the FeVO₄@BiOCl p-n

junction is a highly potential candidate for the abatement of organic contaminants within the alkaline pH range.

3.3.3. Influence of pollutant concentration

In order to unravel the optimal concentration of PNP solution over FeVO₄@BiOCl p-n junction under sonophotocatalytic degradation, the effect of pollutant initial concentration was investigated at 10, 20, 40, 60 and 80 ppm. The degradation of PNP decreased as PNP concentration increased (Fig.S9). The results are supported by a previous study [96]. As the concentration of PNP is increased, the PNP molecules adsorb light, prevent the UV irradiation from reaching the catalyst particles [97] and retard the generation of h⁺ or •OH on the catalyst surface, thus the degradation efficiency decreases. Fig. S9 shows that a 20-ppm concentration of PNP has the best degradation.

3.4. Stability and recyclability

To investigate the stability and reusability of FeVO₄@BiOCl p-n junction, cycling experiments of sonophotocatalytic degradation of PNP were performed. The catalyst was collected using centrifugation, and then dried to be used in several sequential runs under the same operating processes. The sonophotocatalytic performance slightly decreased after six times (Fig.10). This is attributed to the removal of surface contamination and self-cleaning of the catalyst surface provided by the (US) irradiation, keeping the catalyst reactive for longer periods with high reusability and superior stability. Furthermore, the sonophotocatalytic stability of the FeVO₄@BiOCl p-n junction is also indicated by its XRD, which shows no change in the diffraction pattern after the first and six runs in comparison to the virgin as shown in Fig.S10. Thus, all these results confirm that the structure of the FeVO₄@BiOCl p-n junction is sufficiently

stable under reaction conditions, and is a promising candidate for viable use in environmental applications.

3.5. PNP Mineralization

To estimate the extent of mineralization of PNP, TOC analysis was conducted (FigS11). The TOC removal of PNP by the FeVO₄@BiOCl p-n junction reaches 89% after 40 min of sonophotocatalytic irradiation. The significant TOC removal can be attributed to the increased mass transfer enhanced the surface area and increased the active sites of the catalyst, which was produced through the cavitation process [98]. Also, the high performance of charge carriers with a high generation rate of $\cdot\text{OH}$ and $\text{O}_2^{\cdot-}$ radicals enhances TOC removal. This could be attributed to the formation of photoactive complexes between Fe^{3+} and the carboxylic acid intermediates [17]. It is believed that the high value of TOC removal indicated the low concentration of intermediate in the solution after sonophotocatalytic irradiation [99].

3.6. Radical trapping

To unfold the mechanism of the sonophotocatalytic degradation of PNP over the FeVO₄@BiOCl core shell heterojunction, trapping experiments were carried out as shown in Fig.11. Different concentrations of scavengers were employed to confirm the major active species during sonophotocatalytic PNP degradation. We introduced isopropanol (IPA, 40 mmol L⁻¹) to scavenge hydroxyl radicals ($\cdot\text{OH}$), ethylene diaminetetraacetic acid (EDTA, 40 mmol L⁻¹) for holes (h^+), benzoquinone (BQ, 4 mmol L⁻¹) for superoxide radicals ($\cdot\text{O}_2^-$) and potassium dichromate (2 mmol L⁻¹) for electron (e^-). When IPA, EDTA and BQ were introduced, the degradation performance was thoroughly depressed. Conversely, the degradation efficiency of PNP slightly improves with the addition of potassium dichromate, and does not suppress the

degradation performance due to the increased number of surviving holes as a result of trapping the generated electrons. Thus, it can be inferred that $\cdot\text{OH}$, h^+ and $\cdot\text{O}_2$ play dominant roles in sonophotocatalytic degradation and follow the order $\cdot\text{OH} > h^+ > \cdot\text{O}_2$.

4. Conclusions

A core shell $\text{FeVO}_4@ \text{BiOCl}$ p-n junction was successfully fabricated using a facile hydrothermal method. The $\text{FeVO}_4@ \text{BiOCl}$ was employed as both an effective Fenton-like catalyst and an efficient photocatalyst. High performances were demonstrated in the sonophotocatalytic degradation of PNP using a small amount of the catalyst and oxidant in low concentrations within a short time of the combined irradiation system US/UV. A remarkable synergistic effect was observed when the combined US/UV was used. Moreover, the $\text{FeVO}_4@ \text{BiOCl}$ p-n junction possesses superior degradation performance and reusability, even after six cycles of sonophotocatalytic degradation. Moreover, the better mineralization could be achieved with longer irradiation in the US/UV system. In addition, the fabrication of p-n junction in a core shell nanostructure could significantly increase the pH_{pzc} leading to excellent sonophotocatalytic activity in a highly alkaline pH range. The active species-trapping experiments demonstrated that the hydroxyl radicals and holes play a more crucial role than that of super oxide radicals in the degradation performance. A possible mechanism over the $\text{FeVO}_4@ \text{BiOCl}$ p-n heterojunction for the sonophotocatalytic degradation of PNP was proposed. We believe that this work opens up a new application for environmental remediation and energy-harvesting .

References

- [1] JC. Spain, DT. Gibson, Pathway for biodegradation of para-nitrophenol in a *Moraxella* sp. *Appl. Environ. Microbiol.* 57(1991) 812–819.
- [2] F.Z. Yehia, Gh. Eshaq, A.E. ElMetwally, Enhancement of the working pH range for degradation of p-nitrophenol using Fe^{2+} -aspartate and Fe^{2+} -glutamate complexes as modified Fenton reagents, *Egypt. J. Pet.* 25 (2016) 239–245.
- [3] OI. Guliy, OV. Ignatov, OE. Makarov, VV. Ignatovet, Determination of organophosphorus aromatic nitro insecticides and p-nitrophenol by microbial-cell respiratory activity. *Biosens Bioelectron.* 8 (2002) 1005–1013.
- [4] W. Kitagawa, N. Kimura, Y. Kamagata, A novel p-nitrophenol degradation gene cluster from a gram-positive bacterium *Rhodococcus opacus* SAO101. *J. Bacteriol.* 186 (2004) 4894–4902.
- [5] K.P. Mishra, P.R. Gogate, Intensification of sonophotocatalytic degradation of p-nitrophenol at pilot scale capacity, *Ultrason. Sonochem.* 18 (3) (2011) 739-744.
- [6] B. Chakraborty, Kinetic study of degradation of p-nitro phenol by a mixed bacterial culture and its constituent pure strains, *Mater. Today Proc.* 3 (2016) 3505–3524.
- [7] GJ. Zylstra, SW. Bang, LM. Newman, LL. Perry, Biodegradation of Nitroaromatic Compounds and Explosives, *Microbial Degradation of Mononitrophenols and Mononitrobenzoates*. Boca Raton, Florida: Lewis Publishers (2000) 145–160.
- [8] N. Takahashi, T. Nakai, Y. Satoh, Y. Katoh, Variation of biodegradability of nitrogenous organic compounds by ozonation, *Wat Res.* 28 (1994) 1563–1570.
- [9] L. Ai, J. Jiang, Catalytic reduction of 4-nitrophenol by silver nanoparticles stabilized on environmentally benign macroscopic biopolymer hydrogel, *Short Communication, Bioresource Technology* 132 (2013) 374–377.
- [10] M. Samuel, A. Sivaramakrishna, A. Mehta, Bioremediation of p-Nitrophenol by *Pseudomonas putida* 1274 strain, *Journal of Environmental Health Science & Engineering* 12 (2014) 53-60.
- [11] E. Neyens, J. Baeyens, A review of classic Fenton's peroxidation as an advanced oxidation technique, *J. Hazard. Mater.* 98 (2003) 33–50.
- [12] R. Li, Y. Gao, X. Jin, Z. Chen, M. Megharaj, R. Naidu, Fenton-like oxidation of 2, 4- DCP in aqueous solution using iron-based nanoparticles as the heterogeneous catalyst, *J. Colloid Interface Sci.* 438 (2015) 87–93.

- [13] M.A. Oturan, J-J. Aaron, Advanced oxidation processes in water/wastewater treatment: principles and applications. *Crit. Rev. Environ. Sci. Technol.* 44 (2014) 2577–2641.
- [14] M. Jagannathan, F. Grieser, M. Ashokkumar, Sonophotocatalytic degradation of paracetamol using TiO_2 and Fe^{3+} , *Separation and Purification Technology* 103 (2013) 114–118.
- [15] J. Madhavan, F. Grieser, M. Ashokkumar, Combined advanced oxidation processes for the synergistic degradation of ibuprofen in aqueous environments, *J. Hazard. Mater.* 178 (2010) 202–208.
- [16] G.M.S. ElShafei, A. Al-Sabagh, F. Yehia, C. Philip, N. Moussa, G. Eshaq, A. ElMetwally, Metal oxychlorides as robust heterogeneous Fenton catalysts for the sonophotocatalytic degradation of 2-nitrophenol, *Appl. Catal. B: Environ.* 224 (2018) 681–691.
- [17] D. Panda, S. Manickam, Recent advancements in the sonophotocatalysis (SPC) and doped-sonophotocatalysis (DSPC) for the treatment of recalcitrant hazardous organic water pollutants, *Ultrasonics Sonochemistry* 36 (2017) 481–496.
- [18] L. Chen, D. Meng, X. Wu, A. Wang, J. Wang, Y. Wang, M. Yu, In Situ Synthesis of V^{4+} and Ce^{3+} Self-Doped $\text{BiVO}_4/\text{CeO}_2$ Heterostructured Nanocomposites with High Surface Areas and Enhanced Visible-Light Photocatalytic Activity, *J. Phys. Chem. C.* 120 (2016) 18548–18559.
- [19] A. Sobczykński, A. Dobosz., Water Purification by Photocatalysis on Semiconductors, *Pol. J. Environ. Stud.* 10 (4) (2001), 195-205.
- [20] C. Pan, J. Xu, Y. Wang, D. Li, Y. Zhu, Dramatic Activity of $\text{C}_3\text{N}_4/\text{BiPO}_4$ Photocatalyst with Core/Shell Structure Formed by Self-Assembly, *Adv. Funct. Mater.* 22 (2012) 22, 1518–1524.
- [21] Z. F. Bian, J. Ren, J. Zhu, S. H. Wang, Y. F. Lu and H. X. Li, Self-assembly of $\text{Bi}_x\text{Ti}_{1-x}\text{O}_2$ visible photocatalyst with core–shell structure and enhanced activity, *Appl. Catal. B, Environ.* 89 (2009) 577-582.
- [22] Z. C. Xu, Y. L. Hou, S. H. Sun, Magnetic core/shell $\text{Fe}_3\text{O}_4/\text{Au}$ and $\text{Fe}_3\text{O}_4/\text{Au/Ag}$ nanoparticles with tunable plasmonic properties, *JACS* 129 (28) (2007), 8698 –8699.
- [23] H. J. Choi, J. H. Shin, K. Suh, Self-organized growth of Si/Silica/ $\text{Er}_2\text{Si}_2\text{O}_7$ core shell nanowire heterostructures and their luminescence, *Nano Letters*, 5(12) (2005), 2432 –2437.
- [24] A. R. Kortan, R. Hull, R. L. Opila, M. G. Bawendi, M. L. Steigerwald, P. J. Carroll, L. E. Brus, Nucleation and Growth of CdSe on ZnS Quantum Crystallite Seeds, and Vice Versa, in *Inverse Micelle Media*, *J. Am. Chem. Soc.* 112 (1990) 1327-1332.

- [25] D. V. Talapin, I. Mekis, S. Gotzinger, A. Kornowski, O. Benson, H. Weller, CdSe/CdS/ZnS and CdSe/ZnSe/ZnS Core–Shell–Shell Nanocrystals J. Phys. Chem. B 108 (2004) 18826–18831.
- [26] K. Lambert, B. D. Geyter, I. Moreels, Z. Hens, PbTe|CdTe Core|Shell Particles by Cation Exchange, a HR-TEM study, Chem. Mater. 21 (2009) 778–780.
- [27] R. G. Chaudhuri, S. Paria, Core/Shell Nanoparticles: Classes, Properties, Synthesis Mechanisms, Characterization, and Applications, Chem. Rev. 112 (2012) 2373–2433.
- [28] K. M. Parida, A. Nashim, S. K. Mahanta, Visible-light driven Gd₂Ti₂O₇/GdCrO₃ composite for hydrogen evolution. Dalton Trans. 40 (2011) 12839–12845
- [29] C. Shifu, Z. Sujuan, L. Wei, Z. Wei, Preparation and activity evaluation of p–n junction photocatalyst NiO/TiO₂, J. Hazard.Mater. 155 (2008) 320–326
- [30] V.D. Nithya, R.K. Selvan, C. Sanjeeviraja, D.M. Radheep, S. Arumugam, Synthesis and characterization of FeVO₄nanoparticles, Mater. Res. Bull. 46 (2011)1654–1658.
- [31] S.K. Biswas, J.O. Baeg, Enhanced photoactivity of visible light responsive Wincorporated FeVO₄ photoanode for solar water splitting, Int. J. Hydrogen Energy 38 (2013) 14451–14457.
- [32] C.D. Morton, I.J. Slipper, M.J.K. Thomas, B.D. Alexander, Synthesis and characterisation of Fe-V-O thin film photoanodes, J. Photochem. Photobiol. A 216 (2010)209–214.
- [33] L. Huang, X. Wang, J. Yang, G. Liu, J. Han and C. Li, Dual Cocatalysts Loaded Type I CdS/ZnS Core/Shell Nanocrystals as Effective and Stable Photocatalysts for H₂ Evolution, J. Phys. Chem. C, 117(2013),11584-11591.
- [34] A. M. Kusainova, W. Z. Zhou, J. T. Irvine and P. Lightfoot, Layered Intergrowth Phases Bi₄MO₈X (X=Cl, M=Ta and X=Br, M=Ta or Nb): Structural and Electrophysical Characterization, J. Solid State Chem., 166 (2002), 148-157.
- [35] Z.-F. Huang, J. Song, L. Pan, X. Jia, Z. Li, J.-J. Zou, X. Zhang. L. Wang, W₁₈O₄₉ nanowire alignments with a BiOCl shell as an efficient photocatalyst, Nanoscale, 6 (2014), 8865–8872.
- [36] H. Cheng, B. Huang and Y. Dai, Engineering BiOX (X = Cl, Br, I) nanostructures for highly efficient photocatalytic applications, Nanoscale 6 (2014), 2009–2026.
- [37] X. Zhang, X. Liu, C. Fan, Y. Wang, Y. Wang and Z. Liang, A novel BiOCl thin film prepared by electrochemical method and its application in photocatalysis, Appl. Catal. B, Environ. 132 (2013), 332-341.
- [38] H. Wang, L. Zhang, Z. Chen, J. Hu, S. Li, Z. Wang, J. Liu, X. Wang, Semiconductor heterojunction photocatalysts: design, construction, and photocatalytic performances, Chem. Soc. Rev. 43 (2014), 5234-5244.

- [39] D. Hou, X. Hu, P. Hu, W. Zhang, M. Zhang and Y. Huang, Bi₄Ti₃O₁₂ nanofibers-BiOI nanosheets p-n junction: facile synthesis and enhanced visible-light photocatalytic activity *Nanoscale* 5 (20) (2013), 9764-9772.
- [40] Y. Kaneti, Z. Zhang, J. Yue, X. Jiang, A. Yu, Porous FeVO₄ nanorods: synthesis, characterisation, and gas-sensing properties toward volatile organic compounds, *Journal of Nanoparticle Research* 15 (2013) 1948-1963.
- [41] H. Meng, T. Wang, H. Chen, Y. Liu, X. Yu, Y. Zhu, Y. Zhang, BiOCl/SnS₂ core-shell photocatalyst for the degradation of organic pollutants, *NANO: Brief Reports and Reviews*, 8 (2016) 1650087-1650098.
- [42] A.S. Franca, L.S. Oliveira, M.E. Ferreira, Kinetics and equilibrium studies of methylene blue adsorption by spent coffee grounds, *Desalination*. 249 (2009) 267-272.
- [43] V.D. Nithya, R.K. Selvan, C. Sanjeeviraja, D.M. Radheep, S. Arumugam, Synthesis and characterization of FeVO₄ nanoparticles, *Materials Research Bulletin* 46 (2011) 1654–1658.
- [44] T. Lehnen, M. Valldor, D. Niznansky, S. Mathur, Hydrothermally grown porous FeVO₄ nanorods and their integration as active material in gas-sensing devices, *J. Mater.Chem. A*, 2 (2014) 1862–1868.
- [45] K.-L. Zhang, C.-M. Liu, F.-Q. Huang, C. Zheng, W.-D. Wang, Study of the electronic structure and photocatalytic activity of the BiOCl photocatalyst, *Appl. Catal. B Environ.* 68 (2006) 125–129.
- [46] T. Lehnen, M. Valldor, D. Nižňanský, S. Mathur, Hydrothermally grown porous FeVO₄ nanorods and their integration as active material in gas-sensing Devices, *Mater.Chem. A*, 2 (2014) 1862–1868.
- [47] A. S. Vuk, B. Orel, UV-Visible and IR Spectroelectrochemical Studies of FeVO₄ Sol-Gel Films for Electrochromic Applications, *J. Sol-Gel Sci. Techn.* 23 (2002) 165–181
- [48] J. Di, J. Xia, S. Yin, H. Xu, L. Xu, Y. Xu, M. He, H. Li, One-pot solvothermal synthesis of Cu-modified BiOCl via a Cu-containing ionic liquid and its visible-light photocatalytic properties, *RSC Adv.* 4 (2014) 14281–14290.
- [49] K. S. W. Sing, D. H. Everett, R. A. W. Haul, L. Moscou, R. A. Pierotti, J. Rouquerol, T. Siemieniewska, Reporting Physisorption data for Gas/Solid Systems with Special Reference to the determination of surface area and porosity, *Pure Appl. Chem.* 57 (1985) 603 -619.
- [50] S. Brunauer, P.H. Emmett, E. Teller, Adsorption of gases in multimolecular layers, *J. Am. Chem. Soc.*, 60 (1938) 309-319.

- [51] S. Kumar, S. Khanchandani, M. Thirumal, A. K. Ganguli, Achieving Enhanced Visible-Light-Driven Photocatalysis Using Type- II $\text{NaNbO}_3/\text{CdS}$ Core/Shell Heterostructures, *ACS Appl. Mater. Interfaces* 6 (2014) 13221–13233.
- [52] Y. Zhou, C. H. Chen, N. N. Wang, Y. Y. Li, H. M. Ding, Stable Ti^{3+} Self-Doped Anatase-Rutile Mixed TiO_2 with Enhanced Visible Light Utilization and Durability. *J. Phys. Chem. C* 120 (2016) 6116–6124.
- [53] D. Tomova, V. Iliev, A. Eliyas, S. Rakovsky, Promoting the Oxidative Removal Rate of Oxalic Acid on Gold-Doped $\text{CeO}_2/\text{TiO}_2$ Photocatalysts under UV and Visible Light Irradiation. *Sep. Purif. Technol.* 156 (2015) 715–723.
- [54] M. Balamurugan, G. Yun, K.-S. Ahn, S. H. Kang, Revealing the Beneficial Effects of FeVO_4 Nanoshell Layer on the BiVO_4 Inverse Opal Core Layer for Photoelectrochemical Water Oxidation, *J. Phys. Chem.* 121 (2017) 7625–7634.
- [55] J. Su, X.X. Zou, G.D. Li, X. Wei, C. Yan, Y.N. Wang, J. Zhao, L.-J. Zhou, J.S. Chen, Macroporous $\text{V}_2\text{O}_5\text{-BiVO}_4$ Composites: Effect of Heterojunction on the Behavior of Photogenerated Charges. *J. Phys. Chem. C* 2011, 115, 8064–8071.
- [56] H. Q. Wang, Z. B. Wu, Y. Liu, A simple Two-Step Template Approach for Preparing Carbon-Doped Mesoporous TiO_2 Hollow Microspheres. *J. Phys. Chem. C.* 113 (2009) 13317–13324.
- [57] B. Zhou, J. H. Qu, X. Zhao, H. J. Liu, Fabrication and Photoelectrocatalytic Properties of Nanocrystalline Monoclinic BiVO_4 Thin-Film Electrode. *J. Environ. Sci.* 23 (2011) 151–159.
- [58] M. Wang, Q. Liu, Y. S. Che, L. F. Zhang, D. Zhang, Characterization and Photocatalytic Properties of N-Doped BiVO_4 Synthesized via a Sol–Gel Method. *J. Alloys Compd.* 548 (2013) 70–76.
- [59] J. Zhang, J. X. Xia, S. Yin, H. Li, M. H. Xu, M. Q. He, L. Y. Huang, Q. Zhang, Improvement of Visible Light Photocatalytic Activity over Flower-Like $\text{BiOCl}/\text{BiOBr}$ Microspheres Synthesized by Reactable Ionic Liquids. *Colloids Surf. A* 420 (2013) 420, 89–95.
- [60] C. Petrier, M.-F. Lamy, A. Francony, A. Benahcene, B. David, V. Renaudin, N. Gondrexon, Sonochemical Degradation of Phenol in Dilute Aqueous Solutions: Comparison of the Reaction Rates at 20 and 487 kHz *J. Phys. Chem.* 98 (1994) 10514–10520.
- [61] F. Mahmoudkhani, M. Rezaei, V. Asili, M. Atyabi, E. Vaisman, C.H. Langford, A. De Visscher, Benzene degradation in waste gas by photolysis and photolysis-ozonation: experiments and modeling, *Frontiers of Environmental Science & Engineering*, 10 (2016) 1-10.
- [62] F.J. Beltran, *Chemical Degradation Methods for Wastes and Pollutants: Environmental and Industrial Applications*, CRC Press, 1st Edition, 2003.

- [63] A. Mehrdad, R. Hashemzadeh, Ultrasonic degradation of Rhodamine B in the presence of hydrogen peroxide and some metal oxide, *Ultrason. Sonochem.* 17 (2010) 168–172.
- [64] M. Abbasi, N.R. Asl, Sonochemical degradation of Basic Blue 41 dye assisted by nanoTiO₂ and H₂O₂, *J. Hazard. Mater.* 153 (2008) 942–947.
- [65] M.A. Habila, Z.A. AlOthman, A.M. El-Toni, J.P. Labis, M. Soylak, Synthesis and application of Fe₃O₄@SiO₂@TiO₂ for photocatalytic decomposition of organic matrix simultaneously with magnetic solid phase extraction of heavy metals prior to ICP-MS analysis, *Talanta.* 154 (2016) 539–547.
- [66] R.Z. Khaliullin, A.T. Bell, M. Head-Gordon, A density functional theory study of the mechanism of free radical generation in the system vanadate/PCA/H₂O₂, *J. Phys. Chem. B.* 109 (2005) 17984–17992.
- [67] Y.N. Kozlov, G.V. Nizova, G.B. Shul'pin, Oxidations by the reagent O₂–H₂O₂ vanadium derivative–pyrazine-2-carboxylic acid: Part 14. Competitive oxidation of alkanes and acetonitrile (solvent), *J. Mol. Catal. A: Chem.* 227 (2005) 247–253.
- [68] N. Shimizu, C. Ogino, M.F. Dadjour, T. Murata, Sonocatalytic degradation of methylene blue with TiO₂ pellets in water, *Ultrasonics Sonochemistry*, 14 (2007) 184–190.
- [69] R.D.C. Soltani, M. Safari, M. Mashayekhi, Sonocatalyzed decolorization of synthetic textile wastewater using sonochemically synthesized MgO nanostructures, *Ultrason. Sonochem.* 30 (2016) 123–131.
- [70] H. Zhang, C. Wei, Y. Huang, J. Wang, Preparation of cube micrometer potassium niobate (KNbO₃) by hydrothermal method and sonocatalytic degradation of organic dye, *Ultrason. Sonochem.* 30 (2016) 61–69.
- [71] J. Wang, Z. Jiang, L. Zhang, P. Kang, Y. Xie, Y. Lu, R. Xu, X. Zhang, Sonocatalytic degradation of some dyestuffs and comparison of catalytic activities of nano-sized TiO₂, nano-sized ZnO and composite TiO₂/ZnO powders under ultrasonic irradiation, *Ultrason. Sonochem.* 16 (2009) 225–231.
- [72] N. Wetchakun, S. Chaiwichain, B. Inceesungvorn, K. Pingmuang, S. Phanichphant, A. I. Minett, Chen, J. BiVO₄/CeO₂ Nanocomposites with High Visible-Light-Induced Photocatalytic Activity, *ACS Appl. Mater. Interfaces.* 4 (2012) 3718–3723.
- [73] H. W. Huang, L. Y. Liu, Y. H. Zhang, N. Tian, Novel BiIO₄/ BiVO₄ composite photocatalyst with highly improved visible-light-induced photocatalytic performance for rhodamine B degradation and photocurrent generation. *RSC Adv.* 5 (2015) 1161–1167.

- [74] D. Jiang, L. Chen, J. Zhu, M. Chen, W. Shi and J. Xie, Novel p–n heterojunction photocatalyst constructed by porous graphite-like C₃N₄ and nanostructured BiOI: facile synthesis and enhanced photocatalytic activity, *Dalton Trans.*, 42 (2013) 15726-15734.
- [75] W. Zhao, Y. Wang, Y. Yang, J. Tang and Y. N. Yang, Carbon spheres supported visible-light-driven CuO-BiVO₄ heterojunction: Preparation, characterization, and photocatalytic properties, *Appl. Catal. B, Environ.* 115 (2012) 90-99.
- [76] Z. You, C. Wu, Q. Shen, Y. Yu, H. Chen, Y. Su, H. Wang, C. Wu, F. Zhang, H. Yang, A novel efficient g-C₃N₄@BiOI p–n heterojunction photocatalyst constructed through the assembly of g-C₃N₄ nanoparticles, *Dalton Trans.*, 47(2018) 7353-7361.
- [77] R. Vinoth, P. Karthik, K. Devan, B. Neppolian, M. Ashokkumar, TiO₂–NiO p–n nanocomposite with enhanced sonophotocatalytic activity under diffused sunlight, *Ultrason. Sonochem.* 35 (2017) 655–663.
- [78] H. F. Cheng, B. B. Huang, X. Y. Qin, X. Y. Zhang, Y. Dai, A controlled anion exchange strategy to synthesize Bi₂S₃ nanocrystals/BiOCl hybrid architectures with efficient visible light photoactivity, *Chem. Commun.* 48 (2012) 97-99.
- [79] Z. He, Y. Shi, C. Gao, L. Wen, J. Chen, S. Song, BiOCl/BiVO₄ p–n Heterojunction with Enhanced Photocatalytic Activity under Visible-Light Irradiation, *J. Phys. Chem. C.* 118 (2014) 389–398.
- [80] S. Malato, J. Blanco, M. Maldonado, P. Fernández-Ibáñez, A. Campos, Optimising solar photocatalytic mineralisation of pesticides by adding inorganic oxidising species; application to the recycling of pesticide containers, *Appl. Catal. B.* 28 (2000) 163–174.
- [81] A.E. ElMetwally, G.h. Eshaq, A.M. Al-Sabagh, F.Z. Yehia, C.A. Philip, N.A. Moussa, G.M.S. ElShafei, Insight into heterogeneous Fenton-sonophotocatalytic degradation of nitrobenzene using metal oxychlorides, *Sep. Purif. Technol.* 210 (2019) 452–462.
- [82] V.L. Pham, D-G. Kim, S-O. Ko, Oxidative degradation of the antibiotic oxytetracycline by Cu@Fe₃O₄ core-shell nanoparticles. *Sci. Total Environ.* 631–632 (2018) 608–618.
- [83] A. Khataee, R. Soltani, A. Karimi, S. Joo, Sonocatalytic degradation of a textile dye over Gd-doped ZnO nanoparticles synthesized through sonochemical process, *Ultrason. Sonochem.* 23 (2015) 219–230.
- [84] S. Khanchandani, S. Kumar, A. Ganguli, Comparative Study of TiO₂/CuS Core/Shell and Composite Nanostructures for Efficient Visible-Light Photocatalysis, *ACS Sustainable Chem. Eng.* 4 (2016) 1487–1499.
- [85] P.R. Gogate, A.B. Pandit, Sonophotocatalytic reactors for wastewater treatment: A critical review, *AIChE journal.* 50 (2004) 1051-1079.

- [86] M. Mrowetz, C. Pirola, E. Selli, Degradation of organic water pollutants through sonophotocatalysis in the presence of TiO₂, *Ultrason. Sonochem.* 10 (2003) 247–254.
- [87] I. M. Khokhawala, P. R. Gogate, Degradation of phenol using a combination of ultrasonic and UV irradiations at pilot scale operation, *Ultrason. Sonochem.* 17 (2010) 833–838.
- [88] Y. He, F. Grieser, M. Ashokkumar, The mechanism of sonophotocatalytic degradation of methyl orange and its products in aqueous solutions, *Ultrason. Sonochem.* 18 (2011) 974–980
- [89] S.G. Anju, S. Yesodharan, E.P. Yesodharan, Zinc oxide mediated sonophotocatalytic degradation of phenol in water, *Chemical Engineering Journal* 189–190 (2012) 84–93.
- [90] A.M.T. Silva, E. Nouli, A.C. Carmo-Apolinario, N.P. Xekoukoulotakis, D. Mantzavinos, Sonophotocatalytic/H₂O₂ degradation of phenolic compounds in agro-industrial effluents, *Catal. Today* 124 (2007) 232–239.
- [91] A. Verma, H. Kaur, D. Dixit, Photocatalytic, sonolytic and sonophotocatalytic degradation of 4-chloro-2-nitro phenol, *Arch. Environ. Prot.* 39 (2013) 17–28.
- [92] S. Yuan, J. Kang, X. Wu, L. Wang, J. Chen, X. Lu, Development of a Novel Internal Electrolysis System by Iron Connected with Carbon: Treatment of Nitroaromatic Compounds and Case of Engineering Application, *J. of Environ. Eng.* 136 (9) (2010) 975–982.
- [93] V. Augugliaro, M.J. Lopez-Munoz, L. Palmisano, J. Soria, Influence of pH on the degradation kinetics of nitrophenol isomers in a heterogeneous photocatalytic system, *Appl. Catal. A*, 101 (1993) 7–13.
- [94] X. Ou, J. Yan, F. Zhang, C. Zhang, Accelerated degradation of orange G over a wide pH range in the presence of FeVO₄, *Environ. Sci. Eng.* 12(1) (2018) 1–7.
- [95] W.Y. Ahn, S. Sheeley, T. Rajh, D. Cropek, Photocatalytic reduction of 4-nitrophenol with arginine-modified titanium dioxide nanoparticles, *Applied Catalysis B: Environmental* 74 (2007) 103–110.
- [96] A. Khataee, R.D.C. Soltani, A. Karimi, S.W. Joo, Sonocatalytic degradation of a textile dye over Gd-doped ZnO nanoparticles synthesized through sonochemical process, *Ultrason. Sonochem.*, 23 (2015) 219–230. *Ultrason. Sonochem.* 23 (2015) 219–230.
- [97] N. Daneshvar, D. Salari, A. Khataee, Photocatalytic degradation of azo dye acid red 14 in water: investigation of the effect of operational parameters, *J. Photochem. Photobiol. A Chem.* 157 (2003) 111–116.
- [98] S. Taherian, M. Entezari, N. Ghows, Sonocatalytic degradation and fast mineralization of p-chlorophenol: La_{0.7}Sr_{0.3}MnO₃ as a nano-magnetic green catalyst, *Ultrason. Sonochem.* 20 (2013) 1419–1427.

[99] K.H. Wang, Y.H. Hsieh, L.J. Chen, The heterogeneous photocatalytic degradation intermediates and mineralisation for the aqueous solution of cresols and nitrophenols, *J. Hazard. Mater.* 59 (1998) 251–260.